Acta Crystallographica Section A
Foundations of Crystallography
ISSN 0108-7673

Received 30 December 1999
Accepted 3 May 2000

Strategies for structure solution and refinement of small organic molecules from electron diffraction data and limitations of the simulation approach

R. C. Yu,[a]† A. V. Yakimansky,[a]‡ H. Kothe,[a] I. G. Voigt-Martin,[a]* D. Schollmeyer,[b] J. Jansen,[c] H. Zandbergen[c] and A. V. Tenkovtsev[d]

[a]Johannes-Gutenberg-Universität, Institut für Physikalische Chemie, Welder Weg 11, D-55099 Mainz, Germany, [b]Johannes-Gutenberg-Universität, Institut für Organische Chemie, Duesbergweg 10-14, D-55099 Mainz, Germany, [c]Delft University of Technology, Rotterdamseweg 137, 2628 AL Delft, The Netherlands, and [d]Institute of Macromolecular Compounds of the Russian Academy of Sciences, Bolshoi pr. 31, 199004 St. Petersburg, Russia. Correspondence e-mail: voigtmar@mail.uni-mainz.de

In recent years, a series of non-linear optically active bis(benzylidene) ketones have been synthesized and investigated by electron crystallography. In most cases, structure refinement was possible by combining electron diffraction analysis and quantum-mechanical calculations with maximum-entropy methods. However, when the torsional angles between the phenyl rings and the C═C double bonds are strongly affected by the crystal field, this method fails because packing-energy calculations are not sufficiently sensitive. This problem can be solved by refining the approximate model with *SHELXL*, if the data set is sufficiently accurate and the model close to the correct structure. Here it is shown that a considerably superior data set can be obtained at 300 kV with on-line data acquisition.

1. Introduction

In the recent past, bis(benzylidene)cycloalkanones were discovered as perspective non-linear optically active (NLO) chromophores for second-harmonic-generation (SHG) applications (Yakimanski *et al.*, 1997; Kawamata *et al.*, 1996, 1998; Voigt-Martin, Li *et al.*, 1999; Voigt-Martin, Kolb *et al.*, 1999; Voigt-Martin *et al.*, 2000). Extensive studies of their crystalline structures have been performed by us (Yakimanski *et al.*, 1997; Voigt-Martin, Li *et al.*, 1999; Voigt-Martin, Kolb *et al.*, 1999; Voigt-Martin *et al.*, 2000) and other groups (Kawamata *et al.*, 1995, 1998), and possible structure-determining factors have been suggested that are responsible for non-centrosymmetry in the crystal (Kawamata *et al.*, 1998). Measurements of powder SHG efficiencies of a number of 2,6-bis(4-*R*-benzylidene)cyclohexanones have revealed that strong electron donor properties of the substituent *R* is a necessary (but not sufficient) condition for crystal SHG properties (Agrinskaya *et al.*, 1997). In particular, it has been shown that 2,6-bis(4-dimethylaminobenzylidene)cyclohexanone [DMABC, *R* = $-N(CH_3)_2$] possessed very high crystal quadratic non-linearity as estimated by quantum mechanics (Yakimanski *et al.*, 1997; Voigt-Martin, Li *et al.*, 1999) and measured (Kawamata *et al.*, 1998) to be about 50 times that of crystalline urea.

However, some other bis(benzylidene)cycloalkanones, although less SHG active than DMABC but appropriately functionalized for insertion into polymers, either as side-chain or main-chain chromophores, are of particular practical interest. We have determined the crystal structure of one of these SHG chromophores, 2,6-bis(4-hydroxybenzylidene)-cyclohexanone (BHBC, *R* = −OH), and assessed the role of intermolecular hydrogen bonds as the main structure-determining factor for its observed SHG properties (Voigt-Martin, Li *et al.*, 1999).

In this paper, detailed electron diffraction crystal structure analyses of a close analogue of BHBC, 2,6-bis(3-methoxy-4-hydroxybenzylidene)cyclohexanone (BMHBC), is presented. Recently, we managed to synthesize a partially crystalline NLO-active polymer by polycondensation of BMHBC with sebacinoyl chloride (Voigt-Martin, Kolb *et al.*, 1999). Although the BMHBC monomer itself crystallizes in a centrosymmetric space group, as will be shown below, knowledge of the BMHBC crystal structure was of crucial importance for modelling the polymer crystal structure and to be able to

† Permanent address: Institute of Physics, Chinese Academy of Sciences, Beijing 100080, People's Republic of China.
‡ Permanent address: Institute of Macromolecular Compounds of the Russian Academy of Sciences, Bolshoi pr. 31, 199004 St. Petersburg, Russia.

estimate polymer crystal NLO coefficients. It was also important to compare the crystal structures of BHBC and BMHBC, especially their intermolecular hydrogen-bond patterns.

In a number of previous publications, we have emphasized the advantages of electron microscopy, using (i) crystal-packing calculations, (ii) simulation of electron diffraction patterns and (iii) high-resolution imaging and maximum-entropy methods to analyse crystal structures of complicated organic molecules (Voigt-Martin *et al.*, 1995; Voigt-Martin, Li *et al.*, 1999; Voigt-Martin, Kolb *et al.*, 1999; Voigt-Martin *et al.*, 2000). In the present paper, we show the limitations, both general and specific for the molecule under discussion, of the simulation approach and emphasize the conditions under which the simulated approximate crystal structure model can be refined using *SHELXL* (Sheldrick, 1997). We show that such refinement is only possible with such a limited data set if the values are sufficiently accurate. Experiments using 300 kV and on-line data acquisition indicate that the required accuracy can now be obtained experimentally.

2. Sample

Single crystals of 2,6-bis(3-methoxy-4-hydroxybenzylidene)-cyclohexanone (BMHBC) were grown from a 0.5% solution in ethanol. The molecular architecture is indicated in Fig. 1.

Earlier, the close analogue of this molecule, 2,6-bis(4-hydroxybenzylidene)cyclohexanone (BHBC), was studied (Voigt-Martin, Li *et al.*, 1999). Additional electron-donating *m*-OCH_3 substituents in the phenyl rings of BMHBC were thought to increase the molecular non-linearity compared with that of BHBC. However, it will be seen that this small-molecular feature has far-reaching negative consequences on the NLO effect.

3. Methods

3.1. Electron diffraction

For electron diffraction only small crystals of length a few micrometres and thickness about 100 Å are required. These can be grown easily by dissolving BMHBC in ethanol at room temperature, crystallizing for 1 h and subsequently placing some drops of the solution on a mica covered with carbon film. The small crystals were crystallized as the solution slowly evaporated. Then the film with the sample was transferred onto water and picked up by a copper grid from the water surface.

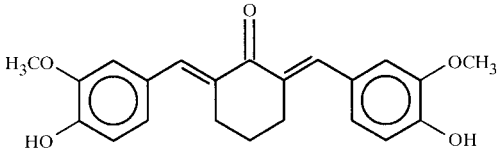

Figure 1
Molecular architecture of BMHBC.

Table 1
Experimental details of X-ray scattering.

Crystal data	
Chemical formula	$C_{22}H_{22}O_5$
Chemical formula weight	366.4
Cell setting	Monoclinic
Space group	$P2_1/c$
a (Å)	15.937 (2)
b (Å)	13.819 (1)
c (Å)	8.288 (1)
β (°)	91.710 (7)
V (Å^3)	1824.5 (3)
Z	4
D_x (Mg m^{-3})	1.334
Radiation type	Cu
Wavelength (Å)	1.54178
No. of reflections for cell parameters	25
θ range (°)	45–59
μ (mm^{-1})	0.770
Temperature (K)	298
Crystal form	Needles
Crystal colour	Yellow–green
Data collection	
Diffractometer	CAD-4
Data-collection method	$\omega/2\theta$ scan
No. of measured reflections	3750
No. of independent reflections	3750
No. of observed reflections	2401
Criterion for observed reflections	$F/\sigma(F) > 4$
R_σ	0.062
θ_{max} (°)	75
Range of h, k, l	$-19 \rightarrow h \rightarrow 19$ $0 \rightarrow k \rightarrow 17$ $0 \rightarrow l \rightarrow 10$
No. of standard reflections	3
Frequency of standard reflections (min)	60
Intensity decay (%)	2
Refinement	
Refinement on	F^2
$R[F^2 > 2\sigma(F^2)]$	0.0588
$wR(F^2)$	0.1654
No. of reflections used for refinement	3750
No. of parameters used	261
Weighting scheme	$w = 1/[\sigma^2(F_o^2 + 0.07P^2 + 0.726P)]$ with $P = (F_o^2 + 2F_c^2)/3$
$(\Delta/\sigma)_{max}$	0.00
$\Delta\rho_{max}$	0.278
$\Delta\rho_{min}$	−0.217
Source of atomic scattering factors	*International Tables for X-ray Crystallography* (1974)

The samples were initially investigated in a Philips EM-300 electron microscope with a eucentric goniometer stage and recorded on film emulsion (Ilford panF) under low-dose conditions. The individual crystals can be rotated and tilted up to ±60°. Details of the experimental procedure have been published in several papers (Voigt-Martin *et al.*, 1995, 1996; Voigt-Martin, Li *et al.*, 1997; Voigt-Martin, Zhang, Kolb & Gilmore, 1997; Voigt-Martin, Zhang, Yan *et al.*, 1997; Voigt-Martin, Li *et al.*, 1999; Voigt-Martin, Kolb *et al.*, 1999; Voigt-Martin *et al.*, 2000; Yakimanski *et al.*, 1997). A short resume is given below.

(i) The basic zone is established by tilting about significant axes and determining the positions corresponding to the largest *d* spacing.

(ii) An axis with strong reflections is established and chosen as the tilt axis. Upon tilting, the diffraction pattern first disappears and reappears when a new zonal projection is reached; the angle is noted and the process is repeated. The tilting is always performed both to the right and to the left directions.

(iii) A second axis is chosen as the tilt axis and the procedure is repeated.

From the diffraction patterns thus obtained, the unit-cell dimensions can be determined. On the basis of observed extinctions, it is generally possible to reduce the number of possible space groups to two or three. During subsequent molecular modelling, the possible number of space groups can normally be further reduced.

The intensities recorded on film emulsion were evaluated initially using the kinematic approximation. In this case, we measure all four quadrants and average symmetry-equivalent reflections. These intensities were used for the direct-methods calculations. Subsequently, the diffraction patterns were recorded by CCD camera and evaluated using *MSLS* (Jansen *et al.*, 1998) taking dynamic effects fully into account.

We have shown previously that by using quantum-chemical calculations combined with simulation methods and maximum-entropy statistics (Voigt-Martin *et al.*, 1995; Voigt-Martin, Li *et al.*, 1999; Voigt-Martin, Kolb *et al.*, 1999; Voigt-Martin *et al.*, 2000; Yakimanski *et al.*, 1997) it is possible to solve and even refine the structure of organic molecules using electron diffraction, despite the fact that quantitative intensity values are acknowledged to be poor and the scattering angle limited.

Model structures can be predicted if there are sufficient restrictions on (*a*) possible molecular conformations due to required bond lengths, torsion angles and symmetry, (*b*) possible crystallographic packing due to van der Waals distances, densities and crystal symmetry. The number of possible molecular conformations

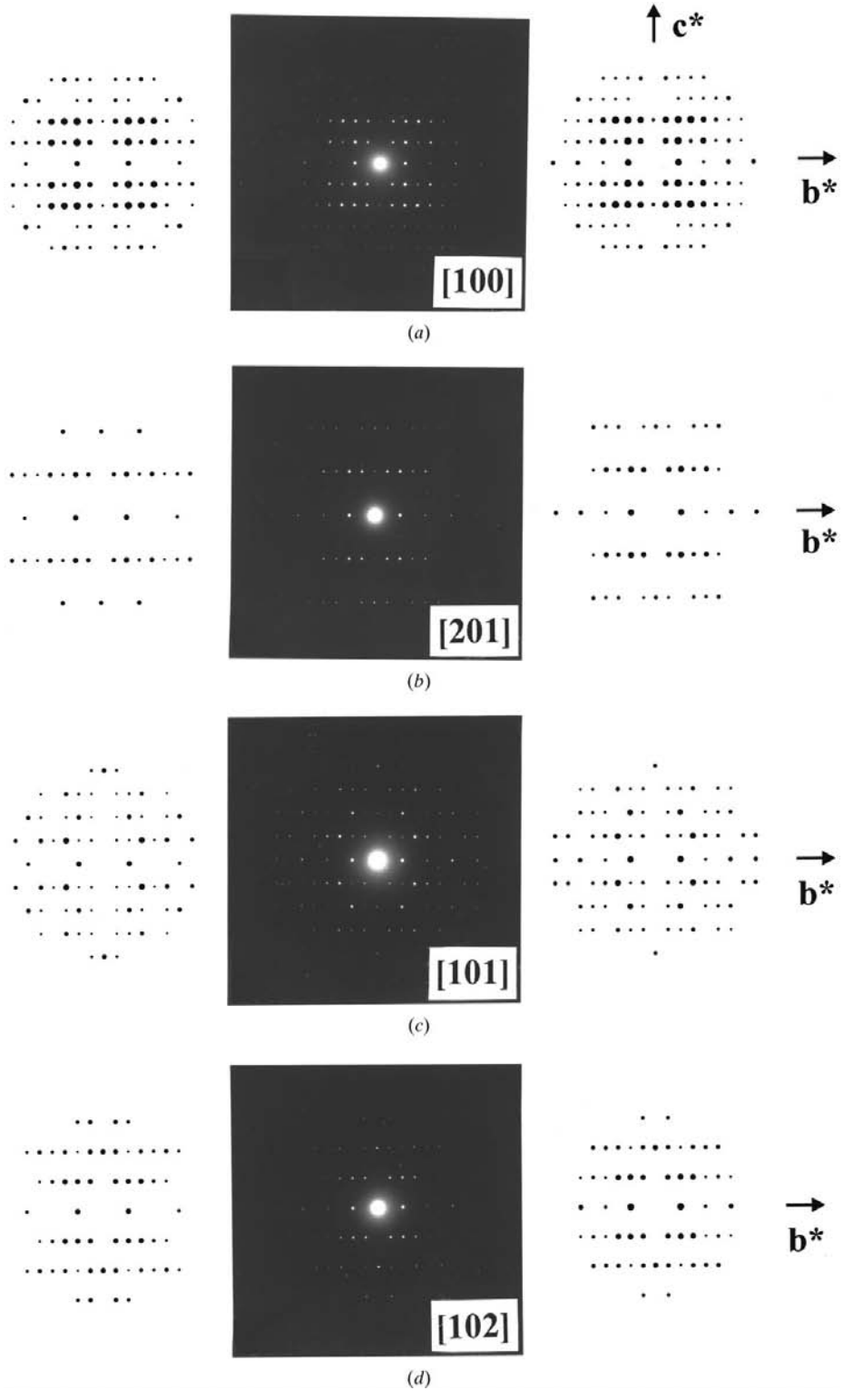

Figure 2
Electron diffraction patterns obtained by tilting along the *b** axis. The middle column shows experimental data. The left-hand and right-hand columns show data simulated from the crystal-packing simulated model and the X-ray model, respectively.

to obtain a negative packing energy is thus strongly restricted. The procedure has been described in detail previously (Voigt-Martin *et al.*, 1995, 1996; Voigt-Martin, Li *et al.*, 1997; Voigt-Martin, Zhang, Kolb & Gilmore, 1997; Voigt-Martin, Zhang, Yan *et al.*, 1997; Voigt-Martin, Li *et al.*, 1999; Voigt-Martin, Kolb *et al.*, 1999; Voigt-Martin *et al.*, 2000; Yakimanski *et al.*, 1997).

3.2. Quantifying the 100 kV electron diffraction data set

The electron diffraction patterns were scanned with a Nikon LS 4500 AF scanner at a resolution of 3000 d.p.i. and transferred to a PC for quantifying using the *ELD* software (Hovmöller, 1992). The procedure is described elsewhere (Voigt-Martin, Li *et al.*, 1999). The quality of the model was assessed by the R value, defined as

$$R = \sum_{hkl} \big||F_o| - |F_c|\big| \Big/ \sum_{hkl} |F_o|.$$

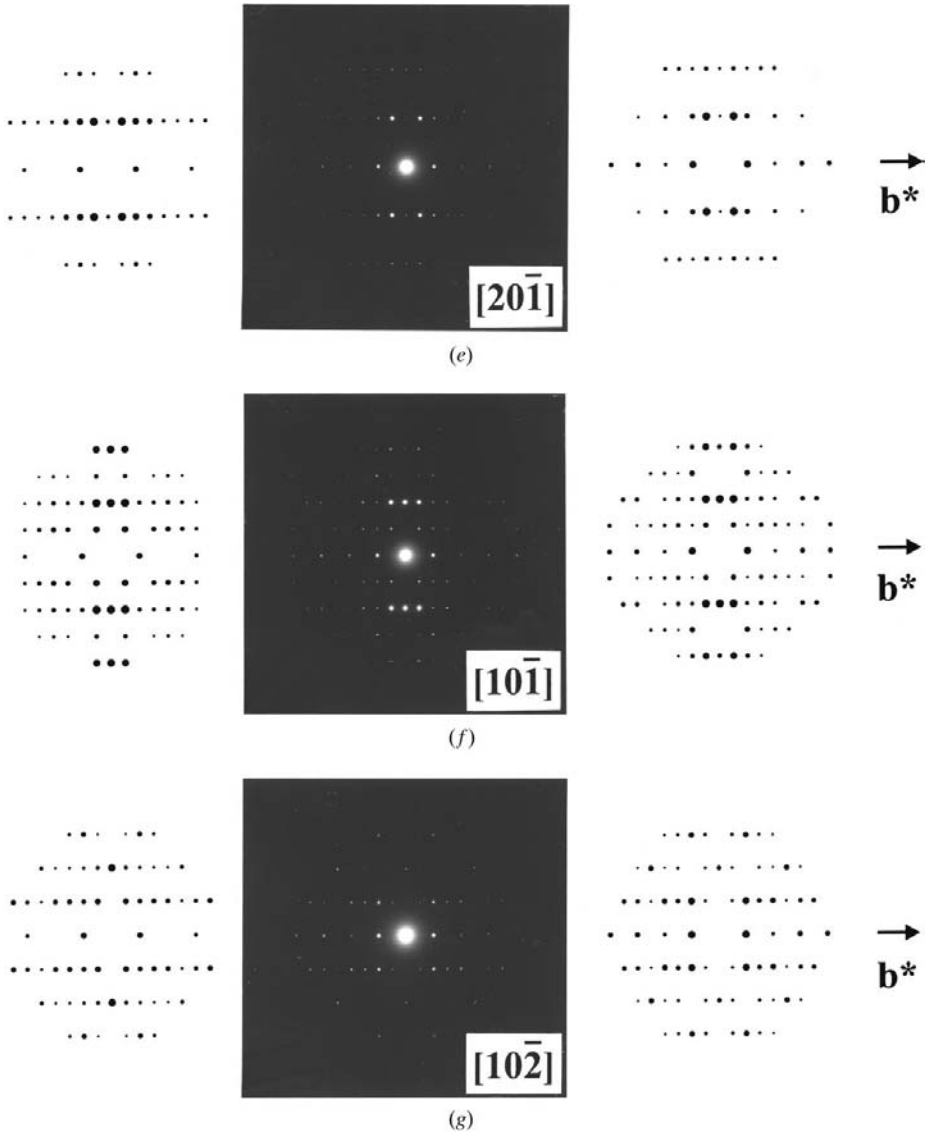

Figure 2 (continued)

3.3. Structure refinement on the 300 kV data

To obtain the most reliable match between observed and calculated data, a full dynamical calculation should be included in the structure refinement. In *MSLS* (Jansen *et al.*, 1998) such a calculation is routinely incorporated. The refinement is based on the following R value,

$$R(I) = \sum[I_m(\text{obs.}) - I_m(\text{calc.})]^2 \Big/ \sum[I_m(\text{obs.})]^2.$$

It should be noted that this R value is based on intensities and that all the reflections have the same weight. The use of intensities I rather than structure factors F is in accordance with the current trend in X-ray crystallography. For comparison reasons, we also calculated (without any refinement) $R(I^{1/2})$, *i.e.*

$$R(I^{1/2}) = \sum[I_m(\text{obs.})^{1/2} - I_m(\text{calc.})^{1/2}]^2 \Big/ \sum[I_m(\text{obs.})].$$

For kinematic diffraction, the structure factors F are proportional to $I^{1/2}$ but, in electron diffraction, dynamical and secondary scattering must be considered. In this respect, it is not so relevant to talk about structure factors as values that are directly related to the scattering potential.

In X-ray crystallography, weighting schemes are often used. One which is sometimes used is the $1/\sigma(I)$ scheme and is based on statistical considerations only. Owing to Poisson statistics, the weakest reflections have the lowest standard deviations and thus the highest weights. In electron crystallography, where the reflections are measured zone by zone and not reflection by reflection in the Bragg position, this means that reflections with low excitations (mostly high diffraction angles) have low intensities because they are not in Bragg position. Applying a $1/\sigma(I)$ weighting scheme for these reflections will introduce a systematic bias in the overall weighting scheme. Owing to the damping caused by the deviation from the Bragg position, such reflections may contain only limited useful structural information. Thus, if these reflections are given high weights, this would mainly add noise. At the moment, the unit weights seem to be better than the $1/\sigma(I)$ scheme but the development of a good weighting scheme for electron diffraction data is a topic for further research.

3.4. Simulation of electron diffraction patterns

To proceed with the simulations, the crystal unit cell and space group is required. This information is obtained from the electron diffraction data combined with X-ray powder results. Generally, several space groups can be postulated on the basis of the observed extinctions. The number can normally be reduced if the symmetry requirements of the molecule and the unit cell are considered in the estimation. For simulation of diffraction patterns, the molecule in the *ab initio* calculated gas-phase conformation (see §3.7) is placed into the unit cell with the required symmetry using the *CERIUS2.0* program (Molecular Simulations, 1996). In recent years, we have found that the maximum-entropy-calculated centroid maps give a very good indication of the molecular envelope, and thus of the molecular orientation with respect to the cell edges. Initial qualitative agreement and a good value of the density can generally be achieved within reasonable time. Further refinement is required to produce a negative packing energy while retaining the correct symmetry. Generally, adjustment of intramolecular rotations and intermolecular orientations are necessary. Details are given in previous papers (Voigt-Martin *et al.*, 1995; Voigt-Martin, Li *et al.*, 1999; Voigt-Martin, Kolb *et al.*, 1999; Voigt-Martin *et al.*, 2000; Yakimanski *et al.*, 1997).

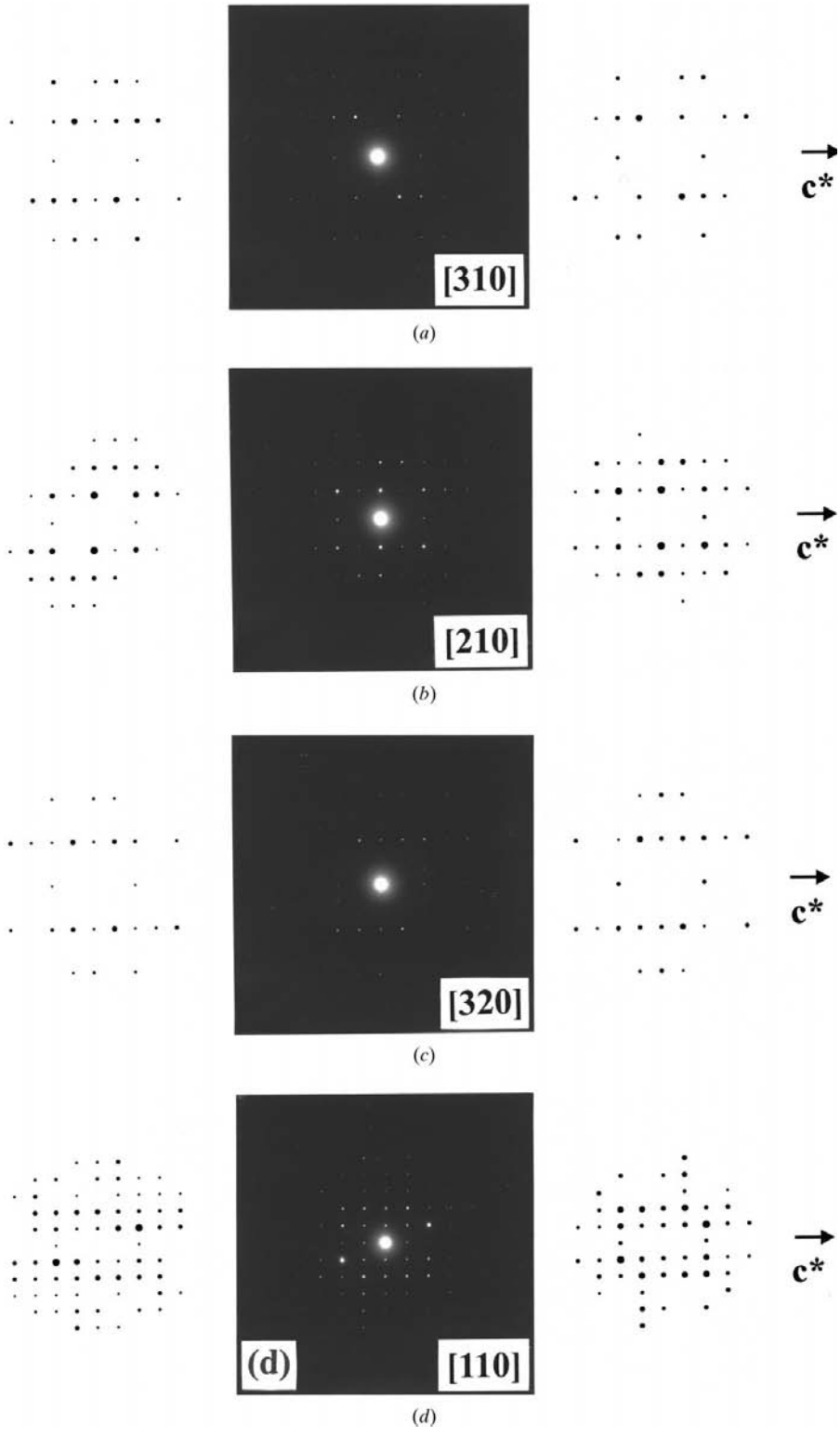

Figure 3
Electron diffraction patterns obtained by tilting along the c^* axis. The middle column shows experimental data. The left-hand and right-hand columns show data simulated from the crystal-packing simulated model and the X-ray model, respectively.

3.5. Maximum-entropy theory

The theoretical concepts involved in the maximum-entropy procedure as used in a crystallographic environment are described in a series of fundamental papers (Bricogne, 1984; Bricogne & Gilmore, 1990; Gilmore *et al.*, 1990; Gilmore & Bricogne, 1997). We have described elsewhere the specific application of the method as applied to another molecule in the present series of bis(benzylidene) ketones (Voigt-Martin, Li *et al.*, 1999).

3.6. High-resolution imaging

High-resolution images were obtained with the Philips EM 420 operating at 120 kV and with a spherical aberration coefficient C_s of 2 mm as described earlier (Voigt-Martin *et al.*, 1995). Imaging beam-sensitive organic samples with this instrument is best achieved by previously adjusting the phase-contrast function for transfer of the required spatial frequencies on an adjacent area of the sample using low-dose facilities.

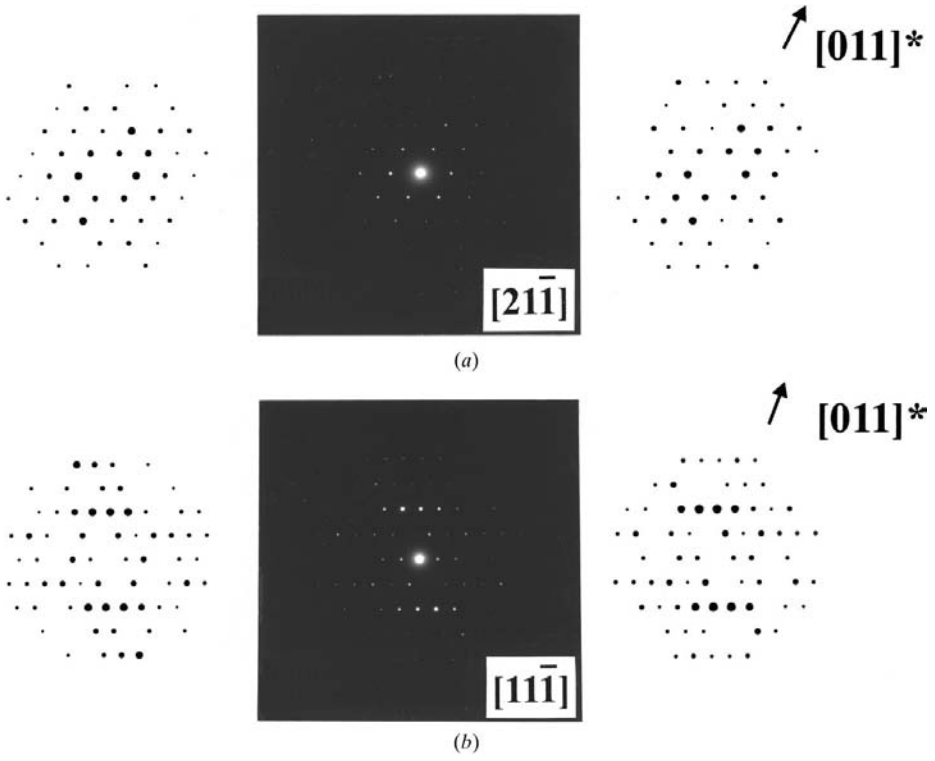

Figure 4
Electron diffraction patterns obtained by tilting along [011]*. The middle column shows experimental data. The left-hand and right-hand columns show data simulated from the crystal-packing simulated model and the X-ray model, respectively.

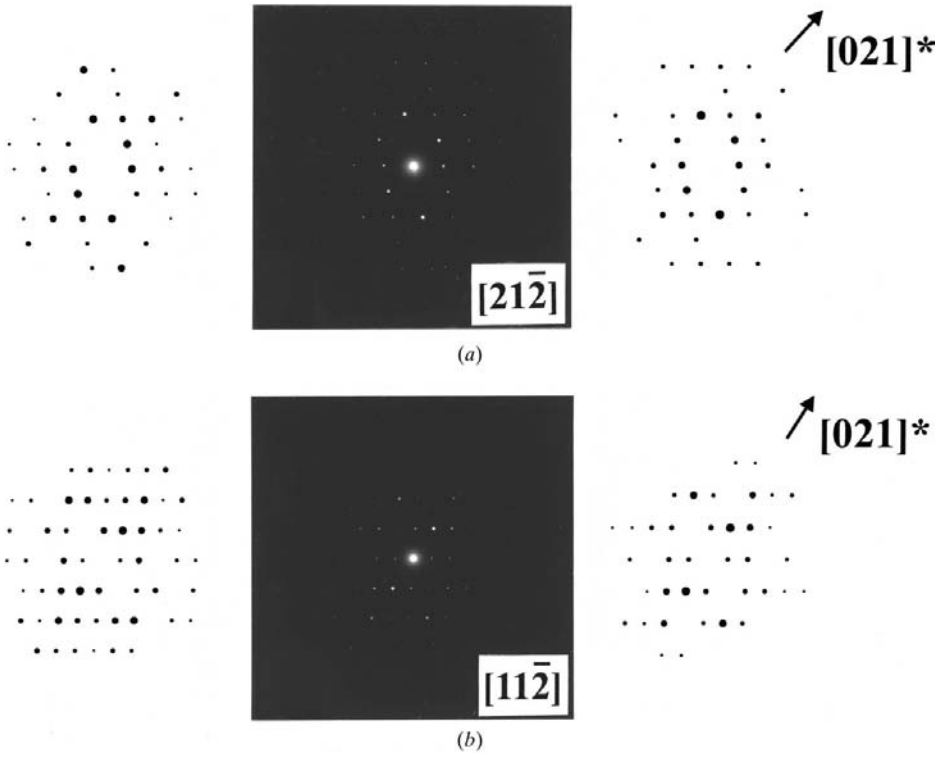

Figure 5
Electron diffraction patterns obtained by tilting along [021]*. The middle column shows experimental data. The left-hand and right-hand columns show data simulated from the crystal-packing simulated model and the X-ray model, respectively.

Although lattice planes cannot always be directly viewed on the monitor, a fast Fourier transform of the image enables a quick decision to be made regarding the suitability of the area in question for imaging and whether the correct transfer function has been chosen. Speed is essential to prevent degradation of the sample in the electron beam. Images taken at 300 kV with a C_s of only 0.5 mm are not always significantly better because beam damage rather than microscope resolution is the decisive factor controlling the quality of images. Work is in progress to optimize the experimental conditions for high-resolution imaging of beam-sensitive samples at 300 kV with a field emission gun.

3.7. X-ray analysis

For X-ray analysis, large single crystals are required and these could not be obtained by the procedure described for electron diffraction. Instead, the BMHBC was dissolved as before but crystallized for two months at room temperature. The experimental details of the X-ray structure analysis are summarized in Table 1.

The structure of these crystals was solved by direct methods using *SIR92* (Altomare *et al.*, 1994) and refined by full-matrix least-squares analysis using *SHELX97* (Sheldrick, 1997). The data were reduced. Lorentz and polarization corrections were applied using a local data-reduction program. Non-H atoms were refined anisotropically, H atoms were placed at geometrically calculated positions and refined isotropically with riding motion.

3.8. Quantum-chemical calculations

The geometry of the BMHBC molecule was completely optimized using a quantum-chemical density functional theory (DFT) *ab initio* approach (Parr & Yang, 1989), implemented into the *TURBOMOLE* program package (Ahlrichs *et al.*, 1989). For the geometry optimization, a split-valence plus polarization (SVP) basis set (Schäfer *et al.*, 1992)

Table 2
Cell parameters obtained from electron diffraction patterns combined with powder X-ray results and single-crystal X-ray measurement.

	a (Å)	b (Å)	c (Å)	α (°)	β (°)	γ (°)
From electron diffraction patterns	15.95 (2)	13.87 (5)	8.42 (1)	90	91.0 (7)	90
From single-crystal X-ray analysis	15.937	13.819	8.288	90	91.71	90

and Becke–Perdew potentials (Becke, 1988; Perdew, 1986) were used.

4. Results and discussion

4.1. Electron diffraction

Very small single crystals (needle shaped, ~3 μm × 0.1 μm × 100 Å) were used for the electron diffraction studies. Figs. 2–5 show the diffraction patterns obtained from tilting along the axes indicated in the diagrams. The diffraction spots in the main zone form a rectangular array. Tilting in positive and negative directions about basic axes gives rise to diffraction patterns that are not identical. The angles between [100] and the successive zones [201], [101], [102], [20$\bar{1}$], [10$\bar{1}$] and [10$\bar{2}$] obtained by tilting along the b^* axis are 15, 28, 47, −14.5, −27 and −45°, respectively. The angles between [100] and [310], [210], [320] and [110] zones obtained by tilting along the a^* axis are 16.5, 23.5, 30 and 41°, respectively, and those between [100] and [21$\bar{1}$], [11$\bar{1}$] zones obtained by tilting along the [011]* axis, and [100] and [21$\bar{2}$], [11$\bar{2}$] zones obtained by tilting along the [021]* axis are 27, 45 and 33.5, 53°, respectively. From this series of patterns, it is clear that the crystal is monoclinic. The observed extinction rules in the experimental diffraction patterns are

$$h0l:\ l = 2n,$$
$$0k0:\ k = 2n.$$

Thus, a $P2_1/c$ space group is a definite possibility. The cell constants can be derived and are shown in Table 2.

4.2. X-ray powder diffraction

X-ray powder measurements were performed using a Siemens D-500 diffractometer in the Θ/2Θ reflection mode (Cu $K\alpha$ radiation with λ = 1.5418 Å). Fig. 6(*a*) shows the X-ray powder diffraction pattern from BMHBC. The above-mentioned extinctions are also shown. Using this pattern, the cell parameters obtained from electron diffraction patterns were refined. They are shown in Table 2. It is clear that there must be four molecules per unit cell to obtain a reasonable density.

4.3. Gas-phase and crystal BMHBC molecular conformations

In order to propose a model and simulate the electron diffraction patterns, the conformation of the molecule is required.

The completely optimized gas-phase BMHBC conformation is shown in Fig. 7(*a*). The torsion angle of the phenyl rings is symmetric with respect to the central C═O double bond, and is found to be ~20°.

4.4. Crystal packing and simulation of electron diffraction patterns

The molecule in the *ab initio* DFT-calculated conformation was placed in the unit cell in such a manner as to satisfy the symmetry and density requirements. Subsequently, the molecular modelling program *CERIUS2.0* was used to calculate and minimize the packing energy including van der Waals, Coulomb and hydrogen-bonding contributions.

Two requirements must be satisfied when performing crystal structure simulations: one is to obtain a reasonable negative packing energy and the other is to obtain the best possible agreement between the experimental and simulated diffraction patterns.

Different molecular conformations (sets of torsion angles), chosen manually around the initial *ab initio* gas-phase conformation, were used as starting models for the crystal-packing energy-minimization procedure. Among crystal structures thus obtained, corresponding to local minima of the packing energy, the optimal structure with regard to the above-mentioned simulation criteria was chosen. This crystal structure is shown in Fig. 8. Its packing energy value is −410 kJ mol^{-1} cell^{-1}. It should be noted that the molecular conformation is non-symmetrical with respect to the central C═O bond (Fig. 7*b*). Namely, torsion angles between the phenyl rings and the C═C double bonds are −42° on one side of the molecule and 3.7° on the other. The atomic coordinates of the model are given in Table 3. For easier comparison with the X-ray model, bond lengths and angles are also compared in Table 3.

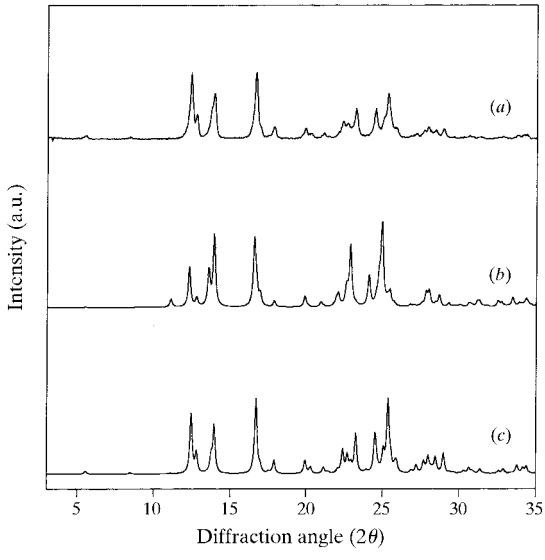

Figure 6
Powder X-ray diffraction patterns. (*a*) Experimental; (*b*) simulated from the packing-energy model; (*c*) simulated from the X-ray model.

Table 3
Atomic coordinates and bond lengths (Å) and angles (°) obtained from different models.

	Simulated model			X-ray model			EM model refined by theoretical data		
	a = 15.95 (2) Å	*b* = 13.87 (5) Å	*c* = 8.42 (1) Å	*a* = 15.937 (2)	*b* = 13.819 (1)	*c* = 8.288 (1) Å	*a* = 15.937 (2) Å	*b* = 13.819 (1) Å	*c* = 8.288 (1) Å
C1	0.5561	0.4578	−0.2412	0.5674 (2)	0.4447 (2)	−0.1976 (3)	0.570 (1)	0.440 (2)	−0.198 (2)
C2	0.4866	0.5028	−0.3135	0.5049 (2)	0.4922 (2)	−0.2844 (3)	0.508 (2)	0.491 (1)	−0.282 (1)
C3	0.4058	0.4826	−0.2604	0.4216 (2)	0.4723 (2)	−0.2558 (3)	0.424 (2)	0.473 (1)	−0.252 (2)
C4	0.3911	0.4159	−0.1360	0.3995 (2)	0.4015 (2)	−0.1435 (3)	0.402 (1)	0.405 (2)	−0.138 (2)
C5	0.4625	0.3715	−0.0620	0.4637 (2)	0.3537 (2)	−0.0563 (3)	0.465 (2)	0.354 (1)	−0.053 (2)
C6	0.5432	0.3923	−0.1136	0.5462 (2)	0.3759 (2)	−0.0830 (3)	0.549 (2)	0.372 (1)	−0.083 (2)
C7	0.3044	0.3995	−0.0912	0.3102 (6)	0.3873 (2)	−0.1140 (3)	0.312 (3)	0.380 (2)	−0.120 (3)
C8	0.2612	0.3177	−0.0515	0.2686 (2)	0.3089 (2)	−0.0627 (3)	0.270 (3)	0.316 (2)	−0.066 (3)
C9	0.1713	0.3335	−0.0057	0.1778 (2)	0.3216 (2)	−0.0315 (3)	0.182 (3)	0.325 (2)	−0.031 (3)
C10	0.1216	0.2483	0.0521	0.1274 (2)	0.2384 (2)	0.0226 (3)	0.120 (3)	0.238 (2)	0.022 (3)
C11	0.1606	0.1488	0.0490	0.1636 (2)	0.1377 (2)	0.0108 (3)	0.164 (2)	0.140 (1)	0.023 (3)
C12	0.2273	0.1401	−0.0790	0.2412 (2)	0.1324 (2)	−0.0924 (4)	0.233 (2)	0.129 (2)	−0.091 (3)
C13	0.2962	0.2161	−0.0546	0.3054 (2)	0.2093 (2)	−0.0408 (4)	0.304 (2)	0.210 (1)	−0.040 (3)
C14	0.0419	0.2688	0.1005	0.0526 (2)	0.2613 (2)	0.0849 (3)	0.055 (3)	0.262 (2)	0.091 (3)
C15	−0.0233	0.2081	0.1671	−0.0107 (2)	0.2047 (2)	0.1661 (3)	−0.019 (1)	0.205 (1)	0.163 (2)
C16	−0.0918	0.2557	0.2407	−0.0795 (2)	0.2572 (2)	0.2228 (3)	−0.084 (1)	0.260 (1)	0.225 (2)
C17	−0.1583	0.2051	0.3082	−0.1409 (2)	0.2131 (2)	0.3114 (3)	−0.143 (1)	0.215 (1)	0.321 (2)
C18	−0.1570	0.1022	0.3063	−0.1352 (2)	0.1142 (2)	0.3450 (3)	−0.137 (1)	0.117 (2)	0.355 (2)
C19	−0.0889	0.0546	0.2377	−0.0687 (2)	0.0617 (2)	0.2876 (4)	−0.072 (2)	0.063 (1)	0.292 (2)
C20	−0.0230	0.1060	0.1686	−0.0064 (2)	0.1057 (2)	0.2000 (4)	−0.013 (1)	0.107 (1)	0.196 (2)
O21	0.6353	0.4764	−0.2892	0.6488 (1)	0.4654 (2)	−0.2271 (3)	0.637 (2)	0.469 (1)	−0.234 (2)
O22	0.6169	0.3554	−0.0519	0.6149 (1)	0.3368 (2)	−0.0032 (3)	0.614 (2)	0.342 (1)	−0.011 (3)
C23	0.6132	0.2900	0.0771	0.6018 (2)	0.2641 (3)	0.1120 (5)	0.602 (2)	0.269 (2)	0.110 (2)
O24	0.1395	0.4150	−0.0116	0.1454 (1)	0.4035 (1)	−0.0438 (3)	0.142 (2)	0.413 (2)	−0.042 (3)
O25	−0.2225	0.0558	0.3739	−0.1958 (1)	0.0742 (2)	0.4360 (3)	−0.194 (2)	0.068 (2)	0.428 (2)
O26	−0.2259	0.2456	0.3785	−0.2087 (1)	0.2594 (2)	0.3738 (8)	−0.212 (3)	0.259 (2)	0.367 (3)
C27	−0.2308	0.3474	0.3854	−0.2087 (2)	0.3620 (3)	0.3710 (5)	−0.208 (2)	0.358 (1)	0.372 (3)

	Simulated model	X-ray model	EM model refined by theoretical data
C1—C2	1.402	1.378 (4)	1.39 (3)
C1—C6	1.425	1.391 (4)	1.39 (3)
C1—O21	1.357	1.357 (3)	1.19 (4)
C2—C3	1.400	1.384 (4)	1.39 (4)
C3—C4	1.421	1.402 (4)	1.39 (3)
C4—C5	1.428	1.401 (4)	1.39 (3)
C4—C7	1.458	1.465 (4)	1.50 (5)
C5—C6	1.397	1.379 (4)	1.39 (4)
C6—O22	1.375	1.370 (3)	1.26 (4)
C7—C8	1.373	1.346 (4)	1.20 (5)
C8—C9	1.508	1.487 (4)	1.45 (7)
C8—C13	1.516	1.505 (4)	1.57 (4)
C9—C10	1.509	1.480 (4)	1.62 (5)
C9—O24	1.240	1.247 (3)	1.37 (5)
C10—C11	1.515	1.511 (4)	1.53 (4)
C10—C14	1.371	1.351 (4)	1.25 (6)
C11—C12	1.534	1.526 (4)	1.48 (5)
C12—C13	1.534	1.529 (4)	1.64 (4)
C14—C15	1.460	1.457 (4)	1.55 (4)
C15—C16	1.428	1.407 (4)	1.39 (3)
C15—C20	1.417	1.398 (4)	1.39 (3)
C16—C17	1.400	1.382 (4)	1.39 (3)
C17—C18	1.428	1.397 (4)	1.39 (3)
C17—O26	1.361	1.370 (3)	1.32 (4)
C18—C19	1.404	1.380 (4)	1.39 (3)
C18—O25	1.361	1.361 (3)	1.30 (3)
C19—C20	1.404	1.388 (4)	1.39 (3)
O22—C23	1.418	1.406 (5)	1.44 (3)
O26—C27	1.416	1.418 (4)	1.36 (3)
C6—C1—C2	119.2	119.9 (2)	120 (2)
O21—C1—C2	121.3	119.0 (2)	110 (2)
O21—C1—C6	119.6	121.1 (2)	130 (2)
C3—C2—C1	119.9	119.8 (2)	120 (2)
C4—C3—C2	122.0	121.0 (2)	120 (2)
C5—C4—C3	117.5	118.5 (2)	120 (2)
C7—C4—C3	117.5	118.0 (2)	119 (2)
C7—C4—C5	125.0	123.3 (2)	121 (2)
C6—C5—C4	120.5	119.9 (2)	120 (2)
C5—C6—C1	120.9	120.8 (2)	120 (2)
O22—C6—C1	112.9	113.3 (2)	110 (2)
O22—C6—C5	126.3	125.9 (2)	130 (2)
C8—C7—C4	132.4	130.7 (2)	139 (3)
C9—C8—C7	115.2	116.8 (2)	124 (3)
C13—C8—C7	125.3	125.4 (2)	123 (3)
C13—C8—C9	119.5	117.7 (2)	113 (3)
C10—C9—C8	118.4	120.1 (2)	126 (3)
O24—C9—C8	120.8	119.7 (2)	121 (3)
O24—C9—C10	120.7	120.2 (2)	113 (3)
C11—C10—C9	119.4	119.0 (2)	113 (3)
C14—C10—C9	115.4	115.3 (2)	116 (3)
C14—C10—C11	125.2	125.7 (2)	129 (3)
C12—C11—C10	111.9	113.4 (2)	115 (2)
C13—C12—C11	110.9	110.9 (2)	107 (2)
C12—C13—C8	112.2	110.3 (2)	111 (2)
C15—C14—C10	131.8	133.0 (2)	134 (3)
C16—C15—C14	117.2	115.8 (2)	117 (2)
C20—C15—C14	125.3	125.9 (2)	122 (2)
C20—C15—C16	117.5	118.1 (2)	120 (1)
C17—C16—C15	122.3	121.4 (2)	120 (1)
C18—C17—C16	119.0	119.6 (2)	120 (2)
O26—C17—C16	125.6	125.0 (2)	123 (2)
O26—C17—C18	115.5	115.4 (2)	116 (2)
C19—C18—C17	119.1	119.4 (2)	120 (2)
O25—C18—C17	117.2	117.7 (2)	124 (2)
O25—C18—C19	123.7	122.9 (2)	116 (2)
C20—C19—C18	121.5	121.3 (2)	120 (2)
C19—C20—C15	120.5	120.1 (2)	120 (1)
C23—O22—C6	118.8	118.5 (2)	116 (2)
C27—O26—C17	118.3	117.5 (2)	115 (3)

Table 4
Calculated R factors from 100 kV data using the X-ray model.

Zone	100	201	101	102	$20\bar{1}$	$10\bar{1}$	$10\bar{2}$	310	210	320	110	$21\bar{1}$	$11\bar{1}$	$21\bar{2}$	$11\bar{2}$	Total
R factor (%)	28.40	20.91	29.72	28.39	29.90	35.88	27.07	28.61	29.38	27.28	27.91	26.53	29.95	28.80	24.91	29.87

Electron diffraction patterns simulated for this structural model (e.d. model) are shown on the left-hand side of Figs. 2–5 together with the corresponding experimental diffraction patterns in the middle.

The X-ray powder diffraction pattern was also simulated from this e.d. model assuming an isotropic distribution of crystals, and is shown in Fig. 6(*b*). Comparing it with that obtained from experiment, there is a slight disparity indicating that the model is not correct. The atomic coordinates corresponding to the simulated structure are presented in Table 2.

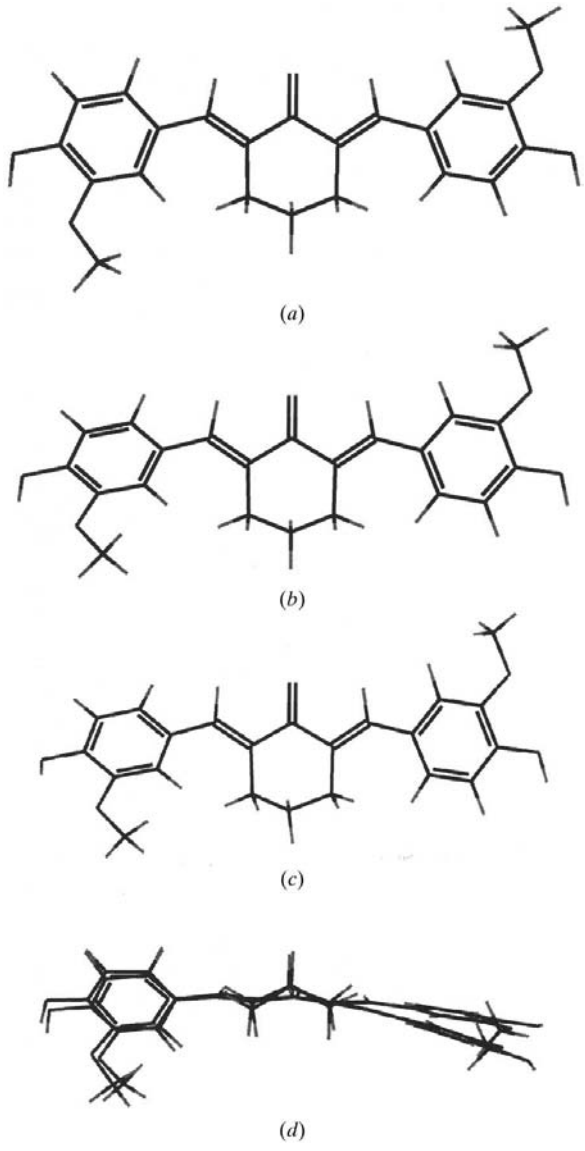

Figure 7
(*a*) *Ab initio* calculated conformation; (*b*) electron diffraction conformation in the crystal; (*c*) X-ray conformation in the crystal; (*d*) superimposed (*b*) + (*c*).

4.5. Quantifying the electron diffraction data

The electron diffraction patterns obtained at 100 kV were scanned with a Nikon LS 4500 AF scanner at a resolution of 3000 d.p.i. and transferred to an IBM 586 computer where they were quantified using *ELD*. In order to overcome the non-linearity of the CCD sensor for optical density, a photographic calibration strip (Kodak 21 strips) was used. Both calibration strip and negatives of three different exposure times for every zone were scanned several times under the same conditions. The CCD calibration was performed using the *ELD* program. Common reflections in the linear regions were used in normalizing. The separate zones were merged into a single set by normalizing medium intensities along common axes. These quantitative values were compared with the kinematical values obtained from the initial e.d. model and the R factor was found to be very high at 49%. It is obvious that the suggested structure (Fig. 8) still requires refinement to reduce this high R-factor value. However, the packing-energy minimization procedure was unable to remove this discrepancy.

4.6. Single-crystal X-ray diffraction

In order to solve this problem, a large crystal suitable for single-crystal X-ray measurements was grown and the structure was determined. The cell constants obtained from the X-ray measurement are also shown in Table 2 and are compared with those obtained by electron diffraction. The crystal space group corresponded to that determined by electron microscopy. The cell parameters are almost the same with tolerable deviations.

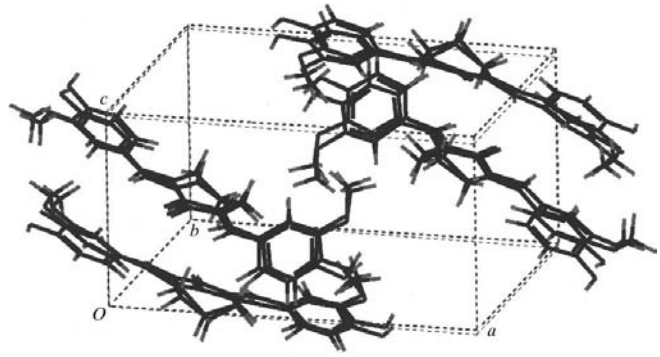

Figure 8
Superimposed structures of the crystal-packing model and the X-ray model.

The atomic coordinates of this structure (X-ray model) are given in Table 3. From these, the molecular conformation in the crystal can be derived. It is shown in Fig. 7(*c*). For easier comparison with the simulated model, the bond lengths and angles of the models are compared in Table 3.

The simulated electron diffraction patterns from this structure are shown in the columns on the right-hand side of Figs. 2–5. The experimental electron diffraction intensities were compared with the theoretical kinematical values obtained from the X-ray model and the *R* factors were calculated for each zone. The results are shown in Table 4. It is clear that this structure corresponds more closely to the electron diffraction data. In order to illustrate the reason for the discrepancy, Fig. 7(*d*) shows an overlap of the molecular conformations in the crystal from packing-energy plus simulation calculations and from X-ray single-crystal analysis. In Fig. 8, the two structures are shown in a manner that highlights both the similarities at the centre of the molecule and the differences at the end groups. At the same time, it also illustrates very clearly the limits of packing-energy calculations for molecules having too many degrees of torsional freedom.

The X-ray powder diffraction pattern was also simulated from this model using *CERIUS2.0*. It is shown in Fig. 6(*c*).

4.7. Maximum-entropy structure determination

The 261 unique electron diffraction intensities were normalized to give unitary structure factors, and three projections along [100], [010] and [001] are shown in Figs. 9(*a*)–9(*c*). The origin-refining reflections 324, 112, 021 were initially given phases of 0°. It is clearly seen from the [010] projection that the four molecules are arranged at an angle with respect to the longest crystal axis in the unit cell. From these potential maps, we can see the approximate arrangements and directions of the molecules in the unit cell. The structure confirms both models because the resolution is not sufficiently good to distinguish between the packing-energy and X-ray models. This is not surprising considering the small differences shown in Fig. 8.

The projections obtained from the simulated electron diffraction model by *CERIUS2.0* are shown in Figs. 9(*d*)–9(*f*) and compared with the maximum-entropy maps. Most of the

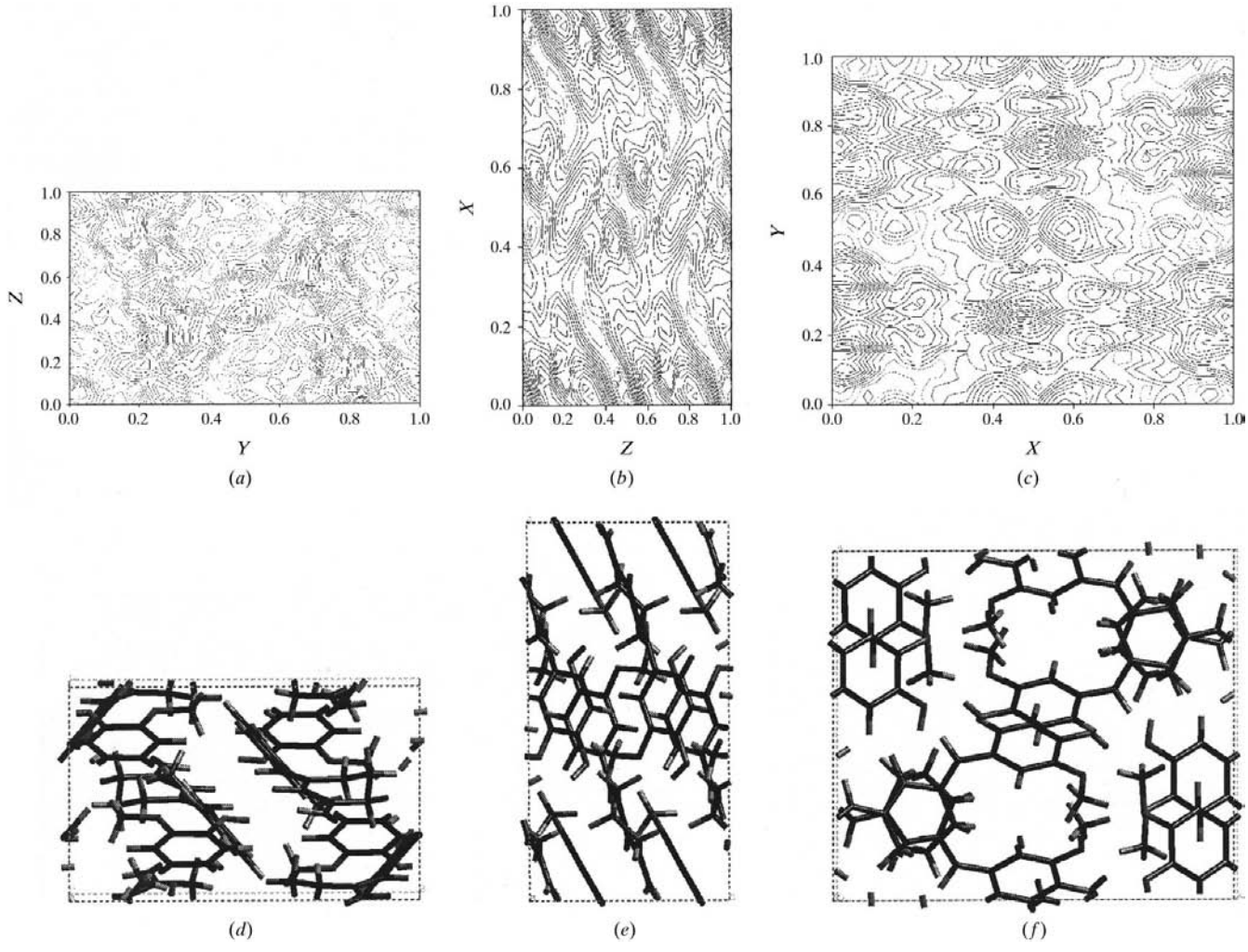

Figure 9
(*a*) [100]; (*b*) [010]; (*c*) [001] maximum-entropy maps obtained using the 261 unique data set; (*d*) [100]; (*e*) [010]; (*f*) [001] projections from the crystal-packing model.

atomic positions in the potential maps correspond to high potential field positions while some of them appear in between high potential regions.

4.8. High-resolution imaging

High-resolution images obtained so far at 300 kV with a field emission gun have not been significantly superior to those obtained at 120 kV because the major limiting factor was beam damage rather than the optical parameters of the microscope. Work is in progress to optimize the experimental procedure. The high-resolution images of the [100] projection obtained at 120 kV are shown in Fig. 10(*b*). Although this image is not of very high quality, the cell information can be obtained from it. Fig. 10(*b*) reveals extensive areas consisting of straight lines with a separation of 13.88 Å (two lines per unit cell). The structures have a high degree of perfection.

The simulated [100] projection of the X-ray single-crystal measurement model is shown in Fig. 10(*a*). Using the X-ray model and the model from packing-energy minimization, simulations of the high-resolution image were performed and are shown in Figs. 10(*c*) and 10(*d*), respectively. The simulated images were calculated by using a slice thickness of 3.99 Å and taking account of the transfer function for a defocus value of −960 Å and a sample thickness of 287 Å. The simulated images agree reasonably with the experimental high-resolution transmission electron microscopy (HRTEM) images. However, the resolution is not sufficiently good to distinguish between the two models.

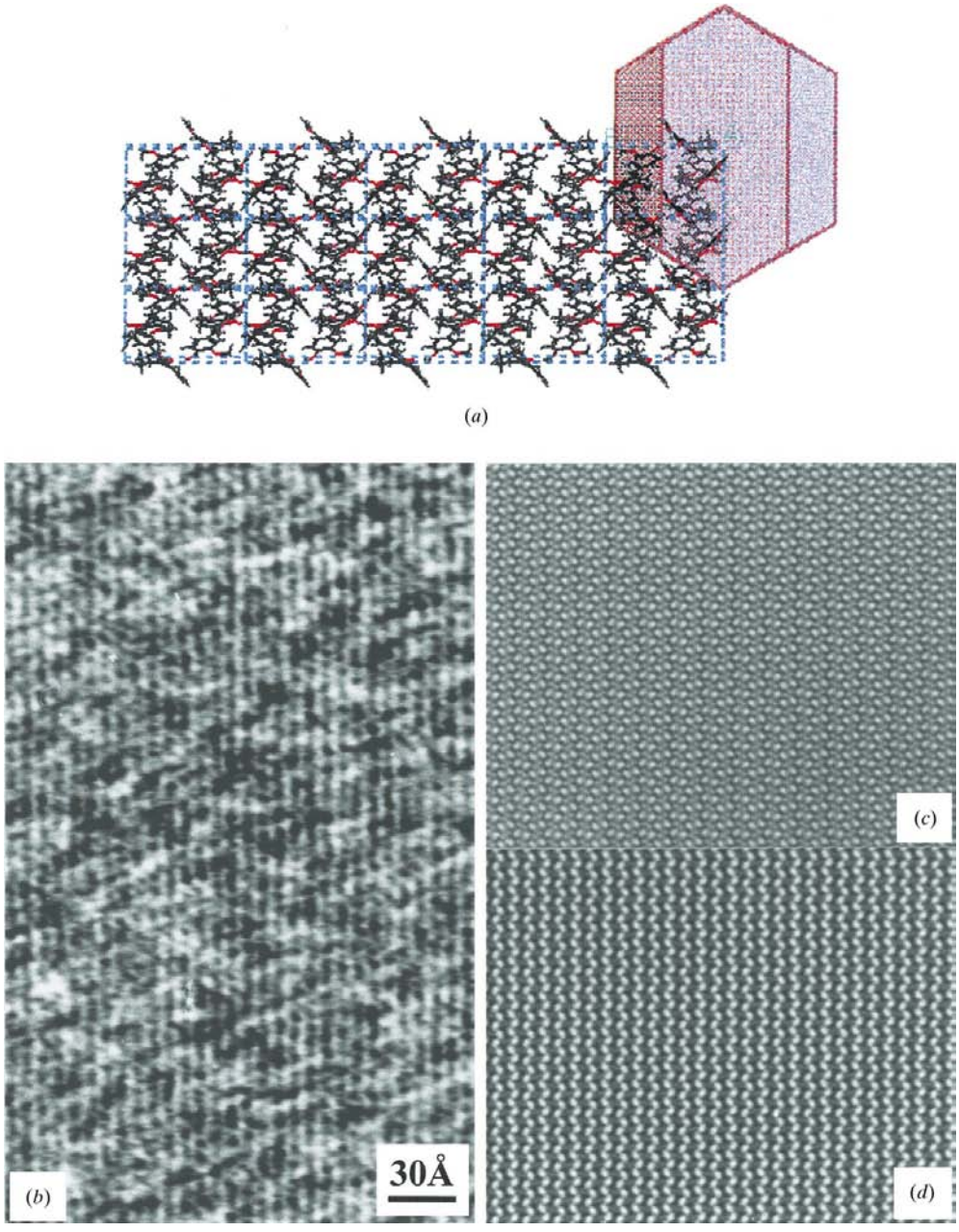

Figure 10
(*a*) [100] projection of the X-ray model combined with the calculated morphology; (*b*) HRTEM image obtained at 120 keV; (*c*) simulated HRTEM image from the X-ray model; (*d*) simulated HRTEM image from the crystal-packing model.

4.9. Use of good electron diffraction data and *SHELX* to refine the model

We have shown that it was not possible to improve the initial e.d. model by further minimizing the packing energy, or with the help of centroid maps, or with high-resolution images. An alternative approach was to see whether the (wrong) model obtained from electron diffraction and packing-energy calculations could be refined using a better data set of reflection intensities, while retaining only the limited-q-range data set corresponding to the 261 reflections that were obtained by electron diffraction. The answer is clearly affirmative. When the 261 theoretical electron diffraction intensities from the correct model are used in *SHELXL* and the (wrong) packing energy model is used as input, then the latter is refined to the correct model. This is shown in Fig. 11, where the two final models are superimposed. In refinement, the electron scattering factors were incorporated into the program. The

phenyl rings were fixed as regular hexagons with d = 1.39 Å and refined as rigid groups. The coordinates of the other non-H atoms were refined free. In this case, the torsional angles were refined. Temperature factors for all atoms were kept fixed (U = 0.05 Å^2 for C, 0.075 Å^2 for methyl H atoms and 0.06 for other H atoms). H atoms were placed at geometrically calculated positions and refined with riding motion.

The maximum positional shift of atoms in our refinement occurred in the early cycles: it was 0.395 Å. The trend of maximum shift became smaller. After some cycles, the refinement converged (shift/e.s.d. = 0.000, maximum shift = 0.000). In our refinement, we did not find distorted geometries. 58 parameters were refined by a data set consisting of 261 unique reflections. The change in R factor was zero after the refinement converged. The atomic coordinates for the refined model are given in Table 3 and the bond lengths and angles are given in Table 3(*a*). It can be seen that there is no molecular distortion. When thermal parameters were not constrained, the refined model was worse than the constrained one and unreasonable thermal parameter values were found. This may be caused by the paucity of data.

This important result shows that good electron diffraction data sets with the inevitable limited set of reflections (261 unique reflections for 196 atoms per unit cell, of which 49 are independent) can be used to solve and refine structures using *SHELXL97*, if the starting model is sufficiently close to the true structure. This starting model can be obtained from packing-energy calculations based on a rather poor agreement with electron diffraction data.

4.10. The 300 kV data set

It was shown in §4.5 that the R factor that was obtained from the 100 kV data using the initial e.d. model was 49%, indicating that the model was wrong. However, the R factors obtained from the correct model were 24–29%. This corresponds to our experience to date. In previous papers (Voigt-Martin, Kolb *et al.*, 1999; Voigt-Martin *et al.*, 2000), it was shown that this value can be considerably reduced by on-line data acquisition at 300 kV. This finding is corroborated here.

Electron diffraction patterns at 300 kV with a specimen temperature of about 100 K were recorded with a 1024 × 1024 pixel camera with a dynamic range of 12 bits. No selected area aperture was used for the selection of the diffraction area but the diameter of the electron beam was limited (diameter $\simeq$ 300 nm). Once a crystal was located, it was scanned by shifting the beam over the specimen with the TEM in diffraction mode. All crystals showed a strong preference for [100] orientation but with a strong buckling over $\sim$20°. Instead of the crystal being tilted to an orientation close to [100], the beam was shifted over the specimen, constantly monitoring the diffraction pattern. Once a crystal area in a misorientation of less than 2° was observed, the diffraction pattern was immediately recorded on the CCD camera, thus reducing the exposure to the electron beam before the actual recording to less than 2 s. Regular checks were performed after 6 s of additional exposure to the beam to determine the rate of loss of information. In general, the diffraction information is significantly reduced in the second exposure.

Because of the buckling of the crystals, a recorded diffraction pattern is likely to come from an area just between two misoriented ones. This implies that the diffraction area itself could also be buckled. This was checked by slight shifts of the beam in the direction of a strong change in orientation. In the diffraction patterns used for the refinements, the variation in orientation is small but is still present in most cases.

The refinement of seven data sets was first performed such that dynamic diffraction was fully taken into account. Only the misorientation and the crystal thickness were refined. The results of the refinements are given in Table 5. The refined misorientations are in agreement with those estimated based on visual inspection of the diffraction patterns. The overall R value of the seven data sets was $R(I)$ = 0.034. Next, two quasi-kinematic refinements were performed. Firstly, the occupancy of all the atom sites was reduced to 1%, which approximates a quasi-kinematic case but with taking into account the Ewald sphere. In a first run, only the misorientation and scale factor were refined. In a second run, the thickness was also refined (see Table 5). As can be seen from Table 5, the R values of this quasi-kinematic refinement are larger than those of the dynamic refinements, showing the importance of the incorporation of dynamic diffraction in the refinement.

However, they are not so large that a quasi-kinematic refinement would fail. A second quasi-kinematic refinement was carried out with a specimen thickness of 1 nm and a site occupancy of 0.01. Compared with the previous quasi-kinematic refinement, the effect of the Ewald sphere (extinction error) is strongly reduced because the reflections are strongly spiked in the [100] direction such that no intensity reduction due to the distance from the Ewald sphere occurs. Only the scale factors were refined in this case. The resulting R values are somewhat higher than those of the other quasi-kinematical refinement (see Table 5).

If in the dynamic refinement the overall Debye–Waller (DW) factor is refined as well, it refines to a value of 11, which is very high. Although the DW factor is rather strongly coupled to the thickness in these refinements (JJ1) (a doubling of the thickness can be largely compensated by a doubling of the DW factors), a fixed DW factor of 4.0 did result in a

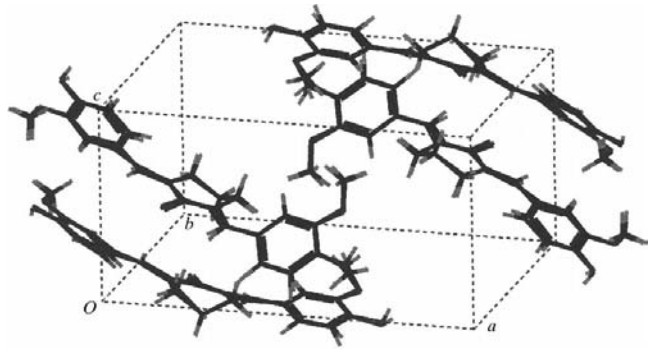

Figure 11
Superimposed structures of the refined model and the X-ray model.

Table 5
The results of various refinements.

The refined thicknesses for the quasi-kinematical refinement fluctuated strongly from refinement to refinement and are therefore not reliable. Data sets DP1–DP4 are from one crystal and data sets DP5–DP7 from another crystal. For all data sets, the misorientation could not be refined leading to a stable parameter.

		DP1	DP2	DP3	DP4	DP5	DP6	DP7
Dynamic refinement	$R(I)$	0.048	0.058	0.032	0.068	0.021	0.018	0.020
	$R(I^{1/2})$	0.087	0.058	0.027	0.084	0.018	0.017	0.019
	Thickness (nm)	23.4 (11)	27.0 (10)	22.8 (9)	22.9 (12)	14.5 (4)	13.5 (6)	12.7 (10)
	Misorientation k	−0.1 (2)	−0.6 (2)	−0.2 (2)	0.3 (2)	0.5 (1)	0.5 (4)	1.3 (5)
	Misorientation l	0.0 (1)	−0.1 (1)	−0.2 (1)	−0.6 (1)	3.9 (2)	3.6 (4)	1.1 (3)
Quasi-kinematic refinement, 'normal thickness', occupancy 0.01	$R(I)$	0.099	0.072	0031	0.154	0.045	0.019	0.047
	$R(I^{1/2})$	0.128	0.127	0.051	0.132	0.023	0.015	0.020
Quasi-kinematic refinement, 1 nm thick, occupancy 0.01	$R(I)$	0.104	0.094	0.048	0.176	0.113	0.042	0.055
	$R(I^{1/2})$	0.072	0.086	0.038	0.092	0.042	0.029	0.018

refinement to approximately the same thicknesses. The high DW factor might be due to the loss of high-frequency information due to structural damage by the electron beam.

The data sets DP1–DP4 in Table 5 are from the same crystal but different areas of this crystal. They all refine to the same thickness range. The data sets DP5–DP7 are from another crystal, again giving similar thicknesses. This indicates that the thickness of the thin crystals is rather homogeneous over a large area of the crystal.

A dynamic refinement of the thickness and misorientation of the seven data sets and the overall DW factor using atomic positions from the e.d. model gave an overall $R(I)$ value of 0.156, which is much higher than the R value obtained with the X-ray diffraction model.

4.11. Comparison of gas-phase and crystal BMHBC conformations

The reason for our inability to obtain a good model for the BMHBC crystal from packing-energy calculations was the difficulty in ascertaining the correct rotation of the torsional angle of the phenyl rings due to the crystal field. This is in marked contrast to the other molecules in this series (Voigt-Martin, Li *et al.*, 1999; Voigt-Martin *et al.*, 2000).

The completely optimized gas-phase conformation of BMHBC is symmetric with respect to the central C═O double bond: torsion angles between phenyl rings and C═C double bonds are ∼20°. However, the molecular conformation, found both in packing-energy calculations and in the X-ray single-crystal structural analysis, is non-symmetric: in the conformation from X-ray analysis, one of the two torsion angles is ∼30° and the other is almost zero. It should be noted that values of these torsion angles are determined by a compromise between the π-electron conjugation (favouring flat conformation) and steric repulsion between aromatic and olefinic protons (favouring strongly torsioned conformation). One possible solution may be symmetrical torsion on both sides of the molecule, and it is the situation that is realized in the gas phase. The other possible compromise is to make the torsion more profound on one side of the molecule and to reduce it (almost up to zero) on the other side. This is the situation realized in the crystal BMHBC structure. Such a non-symmetric conformation did not correspond to a gas-phase potential-energy-surface local minimum. However, the potential-energy surface is rather flat with respect to these torsions: changing the torsion angles by ∼20° leads to only ∼4.2 kJ mol^{-1} change in the total energy. It is reasonable to assume that the non-symmetric BMHBC conformation in the crystal state is induced by the crystal field effect, especially by the intermolecular hydrogen-bonding contribution into the total energy.

4.12. Comparison of BMHBC crystal structure with crystal structures of chemically similar compounds

BMHBC is a representative of 2,6-bis(benzylidene)cycloalkanones, which were recently extensively studied by us (Voigt-Martin, Li *et al.*, 1999; Voigt-Martin *et al.*, 2000) and other groups (Kawamata *et al.*, 1995, 1996, 1998). Some of the compounds of this class, such as 2,6-bis(4-dimethylaminobenzylidene)cyclohexanone (DMABC) (Kawamata *et al.*, 1996, 1998; Agrinskaya *et al.*, 1997; Yakimanski *et al.*, 1997; Voigt-Martin *et al.*, 2000) and 2,6-bis(4-hydroxybenzylidene)-cyclohexanone (BHBC) (Agrinskaya *et al.*, 1997; Voigt-Martin, Li *et al.*, 1999) display a macroscopic NLO SHG effect in the crystal state. In the DMABC crystal structure, which has the largest NLO effect, ∼50 times that of urea (Kawamata *et al.*, 1996), the DMABC molecules occupy special positions in the $Cmc2_1$ space group with the crystal mirror plane passing through the C═O double bond. Thus, the DMABC crystal-state conformation is completely symmetric with respect to the C═O double bond. The BHBC crystal-state conformation is also almost symmetrical, although it is not restricted by its space-group ($Pna2_1$) symmetry conditions. BMHBC is the molecule in this series that has the lowest conformational

symmetry in the crystal state but is nevertheless the only one that crystallizes in a centrosymmetric space group.

Hydrogen-bond-network formation seems to be the main structure-determining factor for both the BHBC and BMHBC crystal structures. In many cases, intermolecular hydrogen bonding in the crystal state leads to a non-centrosymmetric arrangement of molecules and it is explored in SHG-active crystal engineering strategies (Zyss *et al.*, 1984; Etter & Frankenbach, 1989). Unfortunately, this is not the case for the BMHBC crystal structure, in which intermolecular hydrogen bonding resulted in a centrosymmetric structure.

In fact, hydrogen-bonding patterns for the two structures are rather similar. In both structures, there are linear chains of molecules hydrogen-bonded through their terminal OH groups. In the BHBC crystal structure (Fig. 12*a*), these linear chains are along the [010] direction, while in the BMHBC case they are along the $[10\bar{1}]$ direction (Fig. 11*b*). The interchain hydrogen bonds are, in both cases, those between hydroxyl protons in a given chain and carbonyl O atoms in the neighbouring one.

According to a recent suggestion (Kawamata *et al.*, 1998) for 2,6-bis(benzylidene)cycloalkanones, the structure-determining factor mainly responsible for non-centrosymmetric packing is intermolecular hydrogen bonds of the C—H···O type between methylene H atoms in the cycloalkanone ring of one molecule and O atoms of surrounding molecules. Such hydrogen bonds mostly form with carbonyl O atoms as H-atom acceptors. In this case, the C—H···O and H···O═C bond angles are in the range 120–180° (Desiraju, 1991, 1996) and ∼120° (Desiraju, 1996; Bondi, 1964), respectively. No contacts of such type are observed in the BMHBC centrosymmetric crystal structure. In the case of the BHBC non-centrosymmetric crystal, such contacts do exist, but they are between methylene H atoms of a given molecule and hydroxyl O (rather than carbonyl O) atoms of the neighbouring molecule.

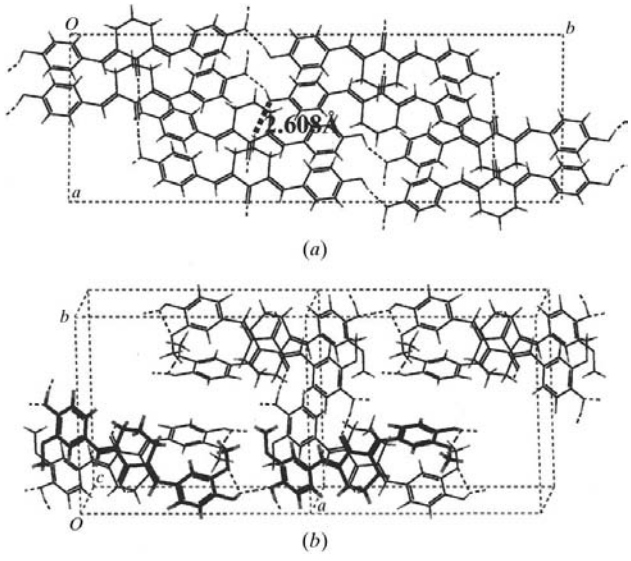

Figure 12
Viewing of the hydrogen-bond chains in (*a*) the BHBC crystal and (*b*) the BMHBC crystal.

5. Conclusions

The limitations of the simulation approach are related to the necessity of packing-energy calculations to find the correct structure. These were performed (i) by using the *Crystal Packer* module of the *CERIUS2.0* program which is a more or less automatic procedure if there is a good guess for the initial atomic positions; (ii) by minimizing the difference between the experimental and observed electron diffraction intensities, which can only be performed by manual adjustment of atomic positions.

As for *Crystal Packer*, the force fields implemented into it cannot be expected to perform well for all types of molecules and crystal structures. Therefore, one cannot expect the program to find the global minimum of the crystal packing-energy multidimensional surface (even localized once) with the accuracy in atomic positions necessary to obtain a good *R* factor. Usually, adjustments based on chemical knowledge need to be made by the operator. In most cases, it is necessary to modify the molecular torsional angles within the molecule manually to try to obtain better agreement between the experimental and observed electron diffraction patterns. However, for molecules with many torsional degrees of freedom, like BMHBC, this manual procedure cannot cover all possible conformations.

In cases where the optimized gas-phase conformation is not significantly affected by the crystal field, we have shown in the past (Voigt-Martin *et al.*, 1995; Voigt-Martin, Li *et al.*, 1999; Voigt-Martin *et al.*, 2000) that this refinement is possible. Unfortunately, BMHBC does not belong to this category.

In many cases, an additional limitation of *Crystal Packer* is that it cannot optimize subrotations within cyclic molecular fragments. However, such subrotations, determining the conformation of *e.g.* cyclohexanone fragments of BMHBC and other 2,6-bis(benzylidene)cyclohexanones, are important for reducing the *R* factor but, unfortunately, can only be estimated.

However, we have shown here that structure determination and refinement is possible from such a limited 100 kV electron diffraction data set using *SHELXL*, provided that the initial model is sufficiently close to the true structure (this can usually be achieved with packing-energy minimization and simulation methods) and if a very good intensity data set is available. We have shown that a dramatic improvement in the *R* factor can be obtained at 300 kV and with on-line CCD data acquisition. These results therefore indicate that a routine use of direct methods to solve and refine the structures of small organic molecules from electron diffraction data is now within reach.

We are extremely grateful to Professor C. Gilmore for giving us free access to his maximum-entropy programs and to the Land Rheinland Pfalz for supporting this project.

References

Agrinskaya, N. V., Lukoshkin, V. A., Tenkovtsev, A. V. & Yakimansky, A. V. (1997). *Solid State Phys.* **39**, 183–188. (In Russian.)

Ahlrichs, R., Bär, M., Häser, M., Horn, H. & Kölmel, C. (1989). *Chem. Phys. Lett.* **162**, 165–169.

Altomare, A., Cascarano, G., Giacovazzo, C., Guagliardi, A., Burla, M. C., Polidori, G. & Camalli, M. (1994). *J. Appl. Cryst.* **27**, 435–436.

Becke, A. D. (1988). *Phys. Rev. A*, **38**, 3098–3100.

Bondi, A. (1964). *J. Phys. Chem.* **68**, 441–451.

Bricogne, G. (1984). *Acta Cryst.* A**40**, 410–445.

Bricogne, G. & Gilmore, C. J. (1990). *Acta Cryst.* A**46**, 284–297.

Desiraju, G. R. (1991). *Acc. Chem. Res.* **24**, 290–296.

Desiraju, G. R. (1996). *Acc. Chem. Res.* **29**, 441–449.

Etter, M. C. & Frankenbach, G. M. (1989). *Chem. Mater.* **1**, 10–12.

Gilmore, C. J. & Bricogne, G. (1997). *Methods Enzymol.* **277**, 65–78.

Gilmore, C. J., Bricogne, G. & Bannister, C. (1990). *Acta Cryst.* A**46**, 297–308.

Hovmöller, S. (1992). *Ultramicroscopy*, **41**, 121–135.

Jansen, J., Tang, D., Zandbergen, H. W. & Schenk, H. (1998). *Acta Cryst.* A**54**, 91–101.

Kawamata, J., Inoue, K. & Inabe, T. (1995). *Appl. Phys. Lett.* **66**, 3102–3104.

Kawamata, J., Inoue, K. & Inabe, T. (1996). *Mol. Cryst. Liq. Cryst.* **278**, 117–124.

Kawamata, J., Inoue, K. & Inabe, T. (1998). *Bull. Chem. Soc. Jpn*, **71**, 2777–2786.

Molecular Simulations (1996). *Cerius2.0 User Guide.* Molecular Simulations, San Diego, USA.

Parr, R. G. & Yang, W. (1989). *Density-Functional Theory of Atoms and Molecules.* Oxford University Press.

Perdew, J. P. (1986). *Phys. Rev. B*, **33**, 8822–8824.

Schäfer, A., Horn, H. & Ahlrichs, R. (1992). *J. Chem. Phys.* **97**, 2571–2577.

Sheldrick, G. M. (1997). *SHELXL97. Program for Crystal Structure Refinement.* University of Göttingen, Germany.

Voigt-Martin, I. G., Kolb, U., Kothe, H., Yakimansky, A. V., Yu, R. C., Matveeva, G. N. & Tenkovtsev, A. V. (1999). *Molecular Order and Mobility in Polymer Systems.* New York: Wiley–VHC.

Voigt-Martin, I. G., Kothe, H., Yakimansky, A. V., Tenkovtsev, A. V., Zandbergen, H., Jansen, J. & Gilmore, C. (2000). *Ultramicroscopy*, **83**, 33–59.

Voigt-Martin, I. G., Li, G., Kolb, U., Kothe, H., Yakimanski, A. V., Tenkovtsev, A. V. & Gilmore, C. (1999). *Phys. Rev. B*, **59**, 6722–6735.

Voigt-Martin, I. G., Li, G., Yakimanski, A., Schulz, G. & Wolff, J. J. (1996). *J. Am. Chem. Soc.* **118**, 12830–12831.

Voigt-Martin, I. G., Li, G., Yakimansky, A., Wolff, J. J. & Gross, H. (1997). *J. Phys. Chem.* **101**, 7265–7276.

Voigt-Martin, I. G., Yan, D. H., Yakimansky, A., Schollmeyer, D., Gilmore, C. J. & Bricogne, G. (1995). *Acta Cryst.* A**51**, 849–866.

Voigt-Martin, I. G., Zhang, Z. X., Kolb, U. & Gilmore, C. (1997). *Ultramicroscopy*, **68**, 43–59.

Voigt-Martin, I. G., Zhang, Z. X., Yan, D. H., Yakimanski, A., Wortmann, R., Matschiner, R., Krämer, P., Glania, C. & Detzer, N. (1997). *Colloid Polym. Sci.* **275**, 18–37.

Yakimanski, A. V., Kolb, U., Matveeva, G. N., Voigt-Martin, I. G. & Tenkovtsev, A. V. (1997). *Acta Cryst.* A**53**, 603–614.

Zyss, J., Nicoud, F. & Coquillay, M. (1984). *J. Chem. Phys.* **81**, 4160–4167.